

# Wavelet-based $L_\infty$ semi-regular mesh coding

Ruxandra Florea\*, Adrian Munteanu\*, *Member, IEEE*, Shao-Ping Lu\*, *Member, IEEE*, Peter Schelkens, *Member, IEEE*

**Abstract**—Polygonal meshes are popular 3D virtual representations employed in a wide range of applications. Users have very high expectations with respect to the accuracy of these virtual representations, fueling a steady increase in the processing power and performance of graphics processing hardware. This accuracy is closely related to how detailed the virtual representations are. The more detailed these representations become, the higher the amount of data that will need to be displayed, stored or transmitted. Efficient compression techniques are of critical importance in this context. State-of-the-art compression performance of semi-regular mesh coding systems has been achieved through the use of subdivision-based wavelet coding techniques. However, the vast majority of these codecs are optimized with respect to the  $L_2$  distortion metric, i.e. the average error. This makes them unsuitable for applications where each input signal sample has a certain significance. To alleviate this problem, we propose to optimize the mesh codec with respect to the  $L_\infty$  metric, which allows for the control of the local reconstruction error. This paper proposes novel data-dependent formulations for the  $L_\infty$  distortion. The proposed  $L_\infty$  estimators are incorporated in a state-of-the-art wavelet-based semi-regular mesh codec. The resulting coding system offers scalability in  $L_\infty$  sense. The experiments demonstrate the advantages of  $L_\infty$  coding in providing a tight control on the local reconstruction error. Furthermore, the proposed data-dependent  $L_\infty$  approaches significantly improve estimation accuracy, reducing the classical low-rate gap between the estimated and actual  $L_\infty$  distortion observed for previous  $L_\infty$  estimators.

**Index Terms**— $L_\infty$  coding, near-lossless compression, semi-regular meshes, subdivision-based wavelets.

## I. INTRODUCTION

Polygonal meshes are one of the most popular examples of 3D virtual representations. Through them, the level of detail in the virtual representation becomes a function of the mesh resolution. Thus, increasing the resolution allows for complying with the available processing power or for adding as much detail as the user requires. The processing power of graphics hardware has witnessed a tremendous increase in the past decades, which in turn triggered a boost in mesh resolution, to the point where virtual objects consisting of millions of vertices are commonplace.

The list of application domains that make use of mesh representations is quite extensive. The one standing out is the popular gaming industry, where the accuracy of the representations translates into commercial success. Nowadays, however, meshes are no longer restricted to

recreational applications. 3D CAD [1] is widely employed in the automobile and aircraft industry. 3D movies, e-learning and telepresence [2] can provide a genuine immersive 3D experience. In turn, they demand highly accurate and realistic 3D representations of humans. These representations require efficient compression before being stored for further use, or transmitted at a remote site for further processing. 3D representations are also employed for the virtual reconstruction of urban or topographic landscapes [3]. 3D mesh geometry watermarking [4-6] offers the means to protect 3D models against copyright violation by embedding imperceptible watermarks in the mesh geometry. Finally, 3D medical imaging can compensate for various inadequacies of classical 2D imaging [7].

Whatever the application environment, handling highly-detailed 3D objects imposes considerable demands in storage, transmission and computational resources. Also, the heterogeneity of existing graphics engines and display terminals requires a quality and resolution-scalable representation of 3D objects. Hence, scalable mesh compression techniques are particularly important. Such techniques offer a range of truncation points for the bit-stream generated by the encoder. Decoding at any of these points generates a coarse version of the input mesh. The more information is provided, the higher the fidelity of the reconstructed mesh. Scalable mesh coding techniques enable efficient compression of 3D meshes, transmission through various environments, rendering on a broad range of end-user terminals with distinct computational capabilities, as well as region-of-interest coding and viewpoint adaptation.

### I.A. State-of-the-art

When covering the literature on scalable mesh coding one first distinguishes technologies that progressively encode the mesh connectivity. Here, we mention well-known methods such as vertex coalescing [8], edge decimation [9] and edge collapsing [10, 11] and consecrated systems such as Progressive Meshes [12, 13] and Topological Surgery [14]. More recent approaches include the state-of-the-art IPR codec of Valette et al. [15], and the FOLProM codec of [16].

Secondly, one distinguished technologies which perform a wavelet-based encoding of the mesh geometry. Here, one may rely on a volumetric wavelet transform, such as our MPEG-4 AFX standardized MeshGrid representation method [17]. Alternatively, one may employ surface wavelets [18]. The state-of-the-art in scalable semi-regular mesh coding systems that deploy wavelets on surfaces is represented by the popular Progressive Geometry Compression (PGC) technique of [19]. PGC relies on the well-known zerotree coding paradigm [20, 21] to encode the wavelet coefficients, and has been adapted in [22] for compression of normal meshes [23]. Other zerotree-based methods [24] have been proposed to support both resolution and quality scalability, though at the cost of compression performance. Other notable semi-regular compression systems include that of Payan et al. [25] which relies on

(\*corresponding author) R. Florea, A. Munteanu, S.-P. Lu, and P. Schelkens are with the Department of Electronics and Informatics, Vrije Universiteit Brussel, Pleinlaan 2, B-1050 Brussels, Belgium (e-mail: [fruxandr@etro.vub.ac.be](mailto:fruxandr@etro.vub.ac.be), [acmunea@etro.vub.ac.be](mailto:acmunea@etro.vub.ac.be), [spLu@etro.vub.ac.be](mailto:spLu@etro.vub.ac.be), [pschelke@etro.vub.ac.be](mailto:pschelke@etro.vub.ac.be)). Tel.: +32-2-629-1693

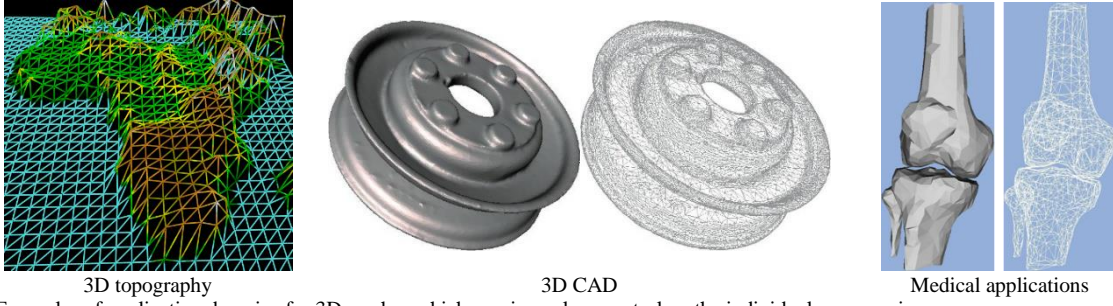


Figure 1: Examples of application domains for 3D meshes which require a close control on the individual compression error.

context-conditioned arithmetic coding and a model-based bit-allocation [26] for calculating the optimal quantizer parameters at each target rate. Recently, we have designed a scalable mesh coding architecture [27] that exploits intraband and composite dependencies between the wavelet coefficients, and offered better compression performance than the state-of-the-art PGC, with comparable complexity.

The vast majority of existing mesh coding techniques [28-34] are optimized with respect to the  $L_2$  metric, and the methods of [17, 19, 22, 24-27] make no exception. The popularity of the  $L_2$  metric is justified by its ability to provide a good approximation of the global error occurring in the lossy compression of the input mesh. However, this same property makes the  $L_2$  metric unsuitable for applications where geometry accuracy is critical at the level of each vertex, such as 3D CAD, coding of topographic surfaces, mesh geometry watermarking, etc.. Both for images and meshes, an alternative has been proposed in the form of the  $L_\infty$  metric, as it allows for imposing a tight bound on the coding error occurring on *each* vertex.

Employing the  $L_\infty$  metric has been studied in the past in the context of image compression. Firstly, we refer to predictive coders operating in the spatial domain. Specifically, methods such as [35, 36] combine uniform quantization with differential pulse-code modulation to ensure an  $L_\infty$  upper bound. Wu et al. have proposed in [37] a near-lossless version of the well-known lossless CALIC [38] which was continued in [39] with a means to correct the prediction biases caused by the quantization of the prediction residues. Finally, the concept of  $L_\infty$  scalability was for the first time introduced in [40]. In addition, there exist a number of transform-domain approaches. Karray et al. [41] follow such an approach, where the  $L_\infty$  upper bound was ensured through the help of confidence intervals. Ansari et al. [42] proposed a hybrid compression scheme composed of a lossy base-layer encoded with an embedded wavelet-based technique and a near-lossless refinement layer encoded using a predictive-based technique. Finally, Chuah et al. [43] aim at improving the  $L_2$  coding performance and rate granularity of  $L_\infty$ -constrained image coding techniques. We note that our research group has a history in wavelet-based  $L_\infty$ -constrained compression of images. In our past work, we have investigated the optimality, in  $L_\infty$  sense, of embedded deadzone scalar quantizers [44], and have introduced efficient  $L_\infty$  image compression systems [45].

In contrast to the image compression domain, the literature for  $L_\infty$ -driven *mesh* compression is very scarce, with publications only from our research group. Specifically, for MeshGrid [17] we have proposed in [46] efficient means to achieve local error control through the use of the  $L_\infty$  metric. Later, in [47, 48] we proposed an  $L_\infty$ -driven extension of the Scalable Intraband Mesh (SIM) coding technique of [27]. In these works we proposed a signal-independent (“theoretical”)  $L_\infty$  distortion estimator which was employed to perform optimized rate allocation. In addition, we proved that the  $L_\infty$  distortion is an efficient

way of controlling the individual reconstruction errors generated by the semi-regular mesh coding architecture. Finally, our method offered  $L_\infty$  scalability. To our knowledge, the techniques of [46-48] are the only ones that investigate local error control in 3D mesh compression.

### I.B. Contributions

The goal of this paper is to design an  $L_\infty$  coding methodology for semi-regular meshes. The proposed approach ensures an accurate control of the coding error on *each* vertex, and presents several novel aspects:

- To our knowledge, we provide the only existing  $L_\infty$ -driven semi-regular mesh coding system;
- We extend our work in [47, 48] through novel data-dependent  $L_\infty$  distortion estimators:
  - We first introduce a data-dependent estimator specifically tailored to semi-regular mesh coding, based on principles described in [46];
  - Next, we propose a novel approach to data-dependent  $L_\infty$  distortion estimation which is experimentally shown to improve estimation accuracy with respect to existing methods;
- Unlike previously-published works, we investigate  $L_\infty$  distortion estimation and  $L_\infty$ -driven coding in the absence of high-rate assumptions.
- Our  $L_\infty$ -driven coding system allows for two separate ways of evaluating the maximum absolute error. First, we define estimators that control the 3D displacement of each vertex. Secondly, the proposed estimators are derived for each coordinate independently, leading to a higher granularity of the encoded bitstream.
- We show that an accurate upper bound for the Hausdorff metric is ensured in  $L_\infty$ -constrained semi-regular mesh compression.
- We provide a system that supports  $L_\infty$  scalability.

The paper is structured as follows. Section 2 describes the employed coding architecture. The  $L_\infty$  coding problem is formulated in Section 3. Section 4 reports the experimental results obtained with our  $L_\infty$ -driven coding approach, whereas Section 5 details some functionalities of the proposed system. Finally, Section 6 draws conclusions, and discusses future directions for our work.

## II. SYSTEM OVERVIEW

The proposed  $L_\infty$  coding system makes use of our Scalable Intraband Mesh (SIM) codec [27] as entropy coding engine and is equipped with the proposed data-dependent  $L_\infty$  distortion estimators in order to accurately control the coding error at the level of each vertex. A brief description of the considered system is given next.

The SIM codec [27] operates on input semi-regular meshes, which are described by a set of vertices in 3D space together with their connectivity. Let  $M$  denote such a mesh, and let  $V = \{v_i = (x_i, y_i, z_i)\}$ ,  $1 \leq i \leq N$ , be the vertex set, with  $N$  denoting the resolution of the input mesh.

The semi-regular input mesh  $M$  undergoes a Butterfly

[49] based multiresolution analysis. Note that employing this transform is common practice in wavelet-based coding of semi-regular meshes, but other transforms can be used in the system as well.

Recursively applying the transform  $J$  times generates  $J$  high-frequency detail subbands  $S_{j=1,\dots,J}$ , which are further processed, and a coarse approximation of the input mesh, i.e. the base mesh  $S_J^A$ . To ensure an accurate reconstruction of the original mesh, the SIM codec losslessly stores the base mesh in the final bit-stream. To this end, common lossless connectivity coders can be used, such as [50].

Each detail subband  $S_j$  is a collection of wavelet coefficients  $c_n^j = (x_n^j, y_n^j, z_n^j)$ ,  $1 \leq n \leq N_j$ , where  $N_j$  is the size of the subband. In general terms, one can view the wavelet coefficients in a given subband as realizations of a random variable  $X$ . The probability distribution function (PDF) of  $X$  can be considered to be a smooth, zero-mean and symmetric function  $f_X(x) = \Pr[X=x]$ ,  $x \in \mathbb{R}$  [26, 27]. In line with the architecture of the SIM codec,  $X$  is quantized with a Successive Approximation Quantizer (SAQ) [51]:

$$q_{\xi, b_j} = \begin{cases} \text{sign}(X) \left\lfloor \frac{|X|}{2^{b_j} \Delta_{j,0}} \right\rfloor & \text{if } \frac{|X|}{2^{b_j} \Delta_{j,0}} > 0 \\ 0 & \text{otherwise} \end{cases} \quad (1)$$

where  $b_j \in \mathbb{Z}_+$  is the quantization level for subband  $S_{j=1,\dots,J}$  and  $\Delta_{j,0}$  is the quantizer bin-size at the highest rate, corresponding to  $b_j=0$ . For any  $S_j$  and  $b_j$ , the deadzone bin-size is equal to  $2^{b_j+1} \Delta_{j,0}$ , while the other bin-sizes are equal to  $2^{b_j} \Delta_{j,0}$ . We note that the maximum quantization error that can be introduced is half the size of the deadzone.

The subsequent SIM coding scheme exploits the intraband statistical dependencies between the wavelet coefficients through octree decomposition and encoding. To further improve compression performance, arithmetic entropy coding is used [27]. Finally, a rate-distortion optimization module allows for minimizing the rate for each imposed upper bound on the estimated distortion. In contrast to the original SIM codec, which optimizes rate allocation with respect to the  $L_2$  distortion, in the proposed system we design and use  $L_\infty$  distortion estimators.

We will later show that the only modules involved in our  $L_\infty$  codec design are the wavelet transform, the quantization and the rate-distortion optimization. Consequently, we will turn our focus to them throughout the rest of this paper without further detailing the octree encoding or the arithmetic entropy coding. They are the same as in the original codec [27]. An in-depth description of the entire SIM compression system can be found in [27].

## II.A. Problem formulation

As described above, the coding system individually encodes each detail subband in a bitplane-by-bitplane manner. Hence, each subband can be regarded as an independent “source of information”. Optimizing the rate allocation implies determining the layers of information (i.e. number of bitplanes) that need to be coded from each source (i.e. subband), such that the required rate is minimized subject to an upper bound on the estimated distortion. Alternatively, one can minimize the distortion subject to a bound on the total rate.

Let  $D_{\text{tot}}$  denote the total reconstruction error in the spatial domain. Each source of information  $j$  has a contribution  $D_j$  to the total distortion, with  $1 \leq j \leq J$ . Typically, one can express the total distortion in the spatial domain as a linear combination of distortion contributions from each source of information [46]:

$$D_{\text{tot}} = \sum_{j=1}^J w_j D_j(R_j) \quad (2)$$

where  $R_j$  is the rate associated with source  $j$ , and  $w_j$  are weights reflecting the contribution of the distortion in subband  $j$ , with respect to the total distortion. For subdivision-based wavelet coding systems, such as [19] or [27], these weights depend only on the wavelet transform of choice and on the type of distortion metric. Concerning the distortion metric, the one originally employed in the SIM codec [27] is the well-known  $L_2$  metric, represented by:

$$\|V - V'\|_2 = \sum_{n=1}^N |v_n - v'_n|^2, \quad (3)$$

where  $V$  is the set of vertices  $v_n$  in the original input mesh and  $V'$  is the set of vertices  $v'_n$  in the decoded mesh. In contrast to [27], in this paper the focus is put on the  $L_\infty$  metric, i.e. the MAXimum Absolute Difference (MAXAD) between the original position of the vertices  $v_n \in V$  and their decoded versions,  $v'_n \in V'$ . We remark here that there are two approaches in the evaluation of the MAXAD.

The first approach computes the maximum 3D displacement of the mesh vertices. In this sense, it computes the Euclidian distance “travelled” by each vertex in 3D space. This approach was followed in our previous work [46-48]. The same number of bitplanes is assumed to be decoded for each coordinate, in line with the original SIM codec implementation [27]. We denote this displacement as  $L_\infty^{\text{Euclidean}}(V, V')$ , where:

$$L_\infty^{\text{Euclidean}}(V, V') = \max_n \left| \sqrt{(v_{x,n} - v'_{x,n})^2 + (v_{y,n} - v'_{y,n})^2 + (v_{z,n} - v'_{z,n})^2} \right| \quad (4)$$

The second approach performs both the evaluation of the MAXAD, and the optimization of the bitplane coding order individually for each component. This “per component” approach leads not only to greater precision in bounding the individual reconstruction error, but to increased granularity as well, as each coordinate will have its dedicated set of decoding points. Hence, this approach requires a modified SIM decoder, in which a different number of bitplanes can be decoded for each coordinate. The decoder can choose the optimal number of bitplanes for each component, such that the imposed upper bound of the MAXAD is respected along each direction. In this sense, the approach is equivalent to computing the per-vertex Chebyshev distance, and taking the maximum across the entire vertex set. We denote this distance as  $L_\infty^{\text{Chebyshev}}(V, V')$ , and define it as:

$$L_\infty^{\text{Chebyshev}}(V, V') = \max_n \left( \max \left( |v_{x,n} - v'_{x,n}|, |v_{y,n} - v'_{y,n}|, |v_{z,n} - v'_{z,n}| \right) \right) \quad (5)$$

Our work incorporates both evaluation methods and experimental results are provided in each case.

## III. DISTORTION ESTIMATORS

### III.A. Data-independent MAXAD estimator [47, 48]

Intuitively, a quantization error produced in a certain wavelet subband will be translated (via wavelet synthesis) into a contribution to the total reconstruction error occurring in the spatial domain. Due to the linear nature of the transform, it is possible to define a linear relation which combines the various quantization errors produced in the detail subbands into corresponding errors in the spatial domain. Under worst-case assumptions, it is then possible to

maximize the different error-contributions from the different wavelet subbands, and determine the smallest upper-bound of the MAXAD. That is, we assume that the quantization errors on individual coefficients are always maximum; furthermore, we assume that (i) these maximum quantization errors *simultaneously* occur on each contributing wavelet coefficient, from each wavelet subband, and (ii) they also have the appropriate sign, depending on the signs of the weights in eq. (2), such that the contributions of the terms in the right side of the equality in (2) are maximized.

In our previous work [47, 48] we followed this methodology and formulated the smallest upper bound  $M_{tot}$  of the MAXAD  $D_{tot}$  for an intraband subdivision-based wavelet coder employing Successive Approximation Quantization [51] as:

$$D_{tot} \leq M_{tot} = \sum_{j=1}^J (K_{S_j^A})^{j-1} \cdot K_{S_j} \cdot \Delta_{j,0} \cdot 2^{b_j} \quad (6)$$

where  $J$  is the total number of decomposition levels, while  $K_{S_j^A}$  and  $K_{S_j}$  are weight factors corresponding to the approximation band  $S_j^A$  and the detail subbands  $S_j, 1 \leq j \leq J$ , respectively. The weight factors are derived from the lifting coefficients. For the unlifted Butterfly transform their values are  $K_{S_j^A} = 1.5$  and  $K_{S_j} = 1$ .

We note that such a data-independent estimator makes no assumptions with respect to the statistics of the input signal. Thus, we can call this estimator to be data-independent, or “theoretical” [47, 48]. We remark that optimizing the coding architecture with respect to this data-independent estimator has the advantage of fast decoding. This is because the wavelet coefficients do not need to be decoded, and no inverse wavelet transform needs to be performed. However, worst-case scenario assumptions come at the cost of over-estimating the *actual*  $L_\infty$  error, in particular at low rates, as it was proven in [47, 48].

An alternative approach is proposed in the following sections, in the form of three distinct “statistical” estimators, i.e. estimators which take into account the statistics of the input signal.

### III.B. Statistical MAXAD estimator

In the formulation of this first statistical estimator we follow the concepts exploited in [46] for a volumetric wavelet transform incorporated in the MeshGrid [27] system. In the following, we rely on these ideas and design an estimator for semi-regular meshes. Though a similar reasoning was presented in [46], we include it here both for comparison to prior work, and to set the theoretical background for the following sections.

Let  $e_{n,b_j}^j$  be a random variable denoting the quantization error occurring on a single wavelet coefficient  $c_n^j$  of subband  $S_j$  at quantization level  $b_j$ . The error contribution of subband  $S_j$  to the total reconstruction error  $e_{tot}$  can be written as:

$$e_{b_j}^j = \sum_n \alpha_n e_{n,b_j}^j,$$

where  $\alpha_n$  are weighting factors depending on the transform.

Under high-rate assumptions, the quantization errors  $e_{n,b_j}^j$  for an arbitrary wavelet subband  $S_j, 1 \leq j \leq J$  are assumed to be uncorrelated. Moreover, the PDF of the input samples can be seen as piecewise uniform in each quantization bin. This implies that the corresponding quantization errors  $e_{n,b_j}^j$  are uniformly distributed on either  $[-2^{b_j} \Delta_{j,0}; 2^{b_j} \Delta_{j,0}]$ , for the deadzone, or on  $[-2^{b_j-1} \Delta_{j,0}; 2^{b_j-1} \Delta_{j,0}]$ , in any other quantization cell. The mean  $\mu_{n,b_j}^j = E\{e_{n,b_j}^j\}$  of such (assumed) uncorrelated and uniformly-distributed variables

$e_{n,b_j}^j$  is zero, while their variance has the expression:

$$(\sigma_{n,b_j}^j)^2 = p_{b_j}^j \frac{1}{12} (2^{b_j+1} \Delta_{j,0})^2 + (1 - p_{b_j}^j) \frac{1}{12} (2^{b_j} \Delta_{j,0})^2, \quad (7)$$

where  $p_{b_j}^j$  represents the probability that  $e_{n,b_j}^j$  is maximum, i.e. that an input coefficient is quantized in the deadzone. Next, the mean of the total subband contribution  $e_{b_j}^j$  is written as:

$$\mu_{b_j}^j = E\{e_{b_j}^j\} = \sum_n \alpha_n E\{e_{n,b_j}^j\} = 0,$$

while the variance  $(\sigma_{b_j}^j)^2$  is given by:

$$(\sigma_{b_j}^j)^2 = \sum_n \alpha_n^2 E\{(e_{n,b_j}^j)^2\} = \sum_n \alpha_n^2 (\sigma_{n,b_j}^j)^2. \quad (8)$$

Using the  $(\sigma_{n,b_j}^j)^2$  in eq. (7) leads to:

$$(\sigma_{b_j}^j)^2 = \sum_n \alpha_n^2 (3p_{b_j}^j + 1) \frac{1}{12} (2^{b_j} \Delta_{j,0})^2 \quad (9)$$

Finally, the standard deviation  $\sigma_{tot}$  of the total reconstruction error  $e_{tot}$  is the cumulated standard deviation of the errors from all subbands, that is:

$$\sigma_{tot}^2 = \sum_j (\sigma_{b_j}^j)^2. \quad (10)$$

with  $(\sigma_{b_j}^j)^2$  computed as in (8).

Let us now assume that the reconstruction error  $e_{tot}$  is upper bounded by an estimated value  $M_{tot}$  with a certain probability  $P \approx 1$ , that is:

$$P = \text{prob}(-M_{tot} < e_{tot} < M_{tot}). \quad (11)$$

According to the assumptions made in the above derivations, the spatial-domain reconstruction error  $e_{tot}$  is a linear combination of identically (here, uniformly) distributed and independent random variables (quantization errors) in each contributing wavelet coefficient from each wavelet subband. In view of the Central Limit Theorem [52],  $e_{tot}$  is Gaussian distributed. Given the Gaussian distribution of  $e_{tot}$ , one can write  $P$  in equation (11) with the help of the error function  $\text{erf}(\cdot)$  as:

$$P = \text{erf}\left(\frac{M_{tot}}{\sigma_{tot} \sqrt{2}}\right) \quad (12)$$

The MAXAD upper bound can now be written in terms of the total standard deviation  $\sigma_{tot}$  as:

$$M_{tot} = \sigma_{tot} \sqrt{2} \text{erf}^{-1}(P), \quad (13)$$

with the estimation probability  $P \approx 1$ .  $\text{erf}^{-1}(P) \geq 9/\sqrt{2}$  was found sufficient when the same number of bitplanes is transmitted across coordinates (with  $M_{tot}$  evaluated as in eq. (4)), while  $\text{erf}_{x,y,z}^{-1}(P) \geq 11/\sqrt{2}$  was sufficient when the estimation / rate allocation are done per coordinate (with  $M_{tot}$  evaluated as in eq. (5)). The MAXAD estimator in eq. (13) is called a data-dependent, or “statistical” estimator, since the data dependencies, i.e. the statistics of the wavelet coefficients, are taken into account.

### III.C. Refined statistical MAXAD estimator

The wavelet coefficients resulting from the wavelet decomposition of a 3D semi-regular mesh can be modeled as having a peaky, symmetric, zero-mean PDF [26, 27]. We propose to incorporate the aforementioned probability model into the design of the estimator.

Given the characteristics of the PDF, the coefficients will fall in the central quantization bin, i.e. the deadzone, with a higher probability than in any other bin. Moreover, one can deduce that (i) samples falling in the central part of the deadzone, i.e.  $[-2^{b_j-1} \Delta_{j,0}; 2^{b_j-1} \Delta_{j,0}]$ , will have quantization errors with a maximum absolute value equal to half the size of any other quantizer cell, and (ii) only samples with values within  $[-2^{b_j} \Delta_{j,0}; -2^{b_j-1} \Delta_{j,0}] \cup (2^{b_j-1} \Delta_{j,0}; 2^{b_j} \Delta_{j,0}]$  will have

quantization errors with a maximum absolute value equal to half the size of the deadzone. This observation lies at the basis of our refined statistical estimator, which we describe next. As before,  $e_{n,b_j}^j$  can be shown to have zero mean. Its variance has the expression:

$$(\sigma_{n,b_j}^j)^2 = \tilde{p}_{b_j}^j (\sigma_{1,b_j}^j)^2 + (1 - \tilde{p}_{b_j}^j) (\sigma_{2,b_j}^j)^2, \quad (14)$$

where  $\tilde{p}_{b_j}^j$  is the probability that a coefficient falls in  $[-2^{b_j} \Delta_{j,0}; -2^{b_j-1} \Delta_{j,0}] \cup (2^{b_j-1} \Delta_{j,0}; 2^{b_j} \Delta_{j,0}]$ , and  $(\sigma_{1,b_j}^j)^2$  is the variance of  $e_{n,b_j}^j$  when uniformly distributed on the aforementioned interval reunion, while  $(\sigma_{2,b_j}^j)^2$  is the variance of  $e_{n,b_j}^j$  when uniformly distributed on  $[-2^{b_j-1} \Delta_{j,0}; 2^{b_j-1} \Delta_{j,0}]$ . Under high-rate assumptions,  $(\sigma_{1,b_j}^j)^2$  can easily be computed as:

$$(\sigma_{1,b_j}^j)^2 = 7 \cdot (2^{b_j} \Delta_{j,0})^2 / 24, \quad (15)$$

while the variance  $(\sigma_{2,b_j}^j)^2$  is:

$$(\sigma_{2,b_j}^j)^2 = (2^{b_j} \Delta_{j,0})^2 / 12. \quad (16)$$

Finally, we are left with determining the value of  $\tilde{p}_{b_j}^j$ . For the statistical estimator presented in the previous section, the probability of a coefficient falling in the deadzone at a certain quantization level could be easily determined at encoding time starting from the binary representation of each quantization index. This, however, will not apply to the refined statistical estimator since the quantization index is the same whether the coefficient (and, implicitly, the quantization error) has a value in  $[-2^{b_j-1} \Delta_{j,0}; 2^{b_j-1} \Delta_{j,0}]$  or in  $[-2^{b_j} \Delta_{j,0}; -2^{b_j-1} \Delta_{j,0}] \cup (2^{b_j-1} \Delta_{j,0}; 2^{b_j} \Delta_{j,0}]$ . For this reason, we propose to simply use a model for the distribution of the input samples. As shown in our past work [27], one can model the distribution  $f_{X_j}(x)$  of the wavelet coefficients in subband  $j$  to be a Laplacian mixture, i.e.:

$$f_{X_j}(x) = \sum_{i=1}^2 a_{j,i} \frac{\lambda_{j,i}}{2} e^{-\lambda_{j,i}|x|} \quad (17)$$

where  $a_{j,1}, a_{j,2}$  are the mixture weights, with  $a_{j,1} + a_{j,2} = 1$ , and  $\sigma_{j,i} = \sqrt{2}/\lambda_{j,i}$  are the standard deviations of the Laplacian distributions in the mixture [27].

We can now compute the probability  $\tilde{p}_{b_j}^j$  as:

$$\tilde{p}_{b_j}^j = \int_{-\Delta_j/2}^{-\Delta_j/2} f_{X_j}(x) dx + \int_{\Delta_j/2}^{\Delta_j/2} f_{X_j}(x) dx = \sum_{i=1}^2 a_{j,i} \int_{\Delta_j/2}^{\Delta_j/2} \lambda_{j,i} e^{-\lambda_{j,i}x} dx \quad (18)$$

which yields:

$$\tilde{p}_{b_j}^j = \sum_{i=1}^2 a_{j,i} (e^{-\lambda_{j,i} \Delta_j/2} - e^{-\lambda_{j,i} \Delta_j}). \quad (19)$$

This approach calls for accurately fitting (at encoding time) the Laplacian mixture on the observed distributions in each subband, and for storing the resulting mixture parameter  $a_{j,1}$  and the Laplacian distribution parameters  $\lambda_{j,i}$  for each wavelet subband.

### III.D. Generalized statistical MAXAD estimator

At high rates, the data-independent (section III.A), and both previous statistical estimators (sections III.B and III.C) yield sufficient accuracy in estimating the actual MAXAD. At low rates, however, one can further improve the estimation accuracy by eliminating their characteristic worst-case, or high rate assumptions. The solution is to determine analytically the actual variances  $(\sigma_{n,b_j}^j)^2$  in (7). Again, we propose to model the distribution of the input samples by means of a Laplacian mixture [27]. The variance  $(\sigma_{b_j}^j)^2$  of the quantization error in the subband  $j$  is given by eq. (8), whereas the variance of the quantization error on

a given coefficient is given by:

$$(\sigma_{n,b_j}^j)^2 = \int_{-2^{b_j} \Delta_{j,0}}^{2^{b_j} \Delta_{j,0}} x^2 f_{X_j}(x) dx + 2 \cdot \sum_{k=1}^{\infty} \int_{k 2^{b_j} \Delta_{j,0}}^{(k+1) 2^{b_j} \Delta_{j,0}} (x - (2k+1) 2^{b_j-1} \Delta_{j,0})^2 f_{X_j}(x) dx \quad (20)$$

Replacing (17) in (20) and changing the variables yields:

$$(\sigma_{n,b_j}^j)^2 = \sum_{i=1}^2 a_{j,i} \lambda_{j,i} \left( \int_0^{\Delta_j} x^2 e^{-\lambda_{j,i}x} dx + (e^{-\lambda_{j,i} \Delta_j/2}) \sum_{k=1}^{\infty} (e^{-\lambda_{j,i} \Delta_j k}) \cdot \int_{-\Delta_j/2}^{\Delta_j/2} x^2 e^{-\lambda_{j,i}x} dx \right), \quad (21)$$

where  $\Delta_j = 2^{b_j} \Delta_{j,0}$  is the cell size at biplane  $b_j$ . Since  $e^{-\lambda_{j,i} \Delta_j} < 1$ , the geometric series in (21) reduces to:

$$\sum_{k=1}^{\infty} (e^{-\lambda_{j,i} \Delta_j k}) = e^{-\lambda_{j,i} \Delta_j} / (1 - e^{-\lambda_{j,i} \Delta_j}) \quad (22)$$

Performing the calculations yields the closed form:

$$(\sigma_{n,b_j}^j)^2 = \sum_{i=1}^2 a_{j,i} \left[ \frac{2}{\lambda_{j,i}^2} - e^{-\lambda_{j,i} \Delta_j} \left( \frac{3\Delta_j^2}{4} + \left( 2 + \coth\left(\frac{\lambda_{j,i} \Delta_j}{2}\right) \right) \frac{\Delta_j}{\lambda_{j,i}} \right) \right] \quad (23)$$

Using these variances, one can then compute the subband contributions (8) and the total estimated MAXAD the same as in (10) and (13).

We note that, compared to previous work on  $L_\infty$ -driven coding, our method is the first to propose a refined and a generalized statistical estimator.

### III.E. Post compression rate-distortion optimization

Apart of accurately estimating the distortion,  $L_\infty$ -oriented coding also requires identifying the optimal number of bitplanes to be transmitted from each wavelet subband such that the bit-rate is minimal for any given user-defined MAXAD bound. The original  $L_2$ -driven SIM codec [27] proposed three predefined bitplane transmission schemes (or progression orders), each targeting resolution and/or quality scalability. However, neither of these subband transmission schemes is necessarily optimal with respect to the  $L_\infty$  distortion, i.e. none minimize the rate given a MAXAD bound. These rate-distortion optimization problems can be solved using Lagrangian optimization techniques, as explained next.

After  $J$  decomposition levels, the intraband bitplane coding scheme generates an embedded bit-stream  $\Pi_j$  for each subband  $S_j$ ,  $1 \leq j \leq J$ . The bitstreams  $\Pi_j$  can be truncated at a predefined set of points  $\tau_{b_j, \Pi_j}$ , where  $b_j$  is the number of discarded bitplanes for the subband  $S_j$ . Each truncation point  $\tau_{b_j, \Pi_j}$  is associated with a certain bitrate  $R_j(b_j)$  and a distortion  $D_j(b_j)$ . One aims at ensuring an optimized performance in rate-distortion sense. This is formulated as a constrained optimization problem, by which the optimal truncation points  $\tau_{b_j, \Pi_j}$  need to be determined such that, in our case, the rate is minimal subject to a constraint on the total distortion.

We note that the  $L_\infty$  metric does not lead to convex problems, due to its non-linear nature. However, employing either of the  $L_\infty$  distortion upper-bounds proposed in sections III.A, III.B, and III.C leads to a convex optimization problem if one considers as eligible truncation points in each subband only those points that lie on the convex hull of the distortion-rate function. In this case, the



TABLE 1  
DECREASE IN DISTORTION  $\Delta D_{j,b_j}$  AND WEIGHTS  $w_j$  CORRESPONDING TO SUBBAND  $j$  AT QUANTIZATION LEVEL  $b_j$ , FOR EACH  $L_\infty$  DISTORTION ESTIMATOR. THE SUBBAND WEIGHTS  $w_j$  ARE COMPUTED FOR THE CASE OF THE UNLIFTED BUTTERFLY WAVELET TRANSFORM.

	$L_\infty$ Data-independent [47, 48]	$L_\infty$ Statistical	$L_\infty$ Refined statistical	$L_\infty$ Generalized statistical
$\Delta D_{j,b_j}$	$2^{b_j} \Delta_{j,0}$	$(\sigma_{b_j}^j)^2$ , eq. (9)	$(\sigma_{b_j}^j)^2$ , using eq. (8) and eq. (14)	$(\sigma_{b_j}^j)^2$ , using eq. (8) and eq. (23)
$w_j$	$(K_{S_j^A})^{j-1} \cdot K_{S_j}$ $K_{S_j^A} = 1.5, K_{S_j} = 1.$	$(K_{S_j^A})^{j-1} \cdot K_{S_j}$ $K_{S_j^A} = 35/64, K_{S_j} = 1.$		

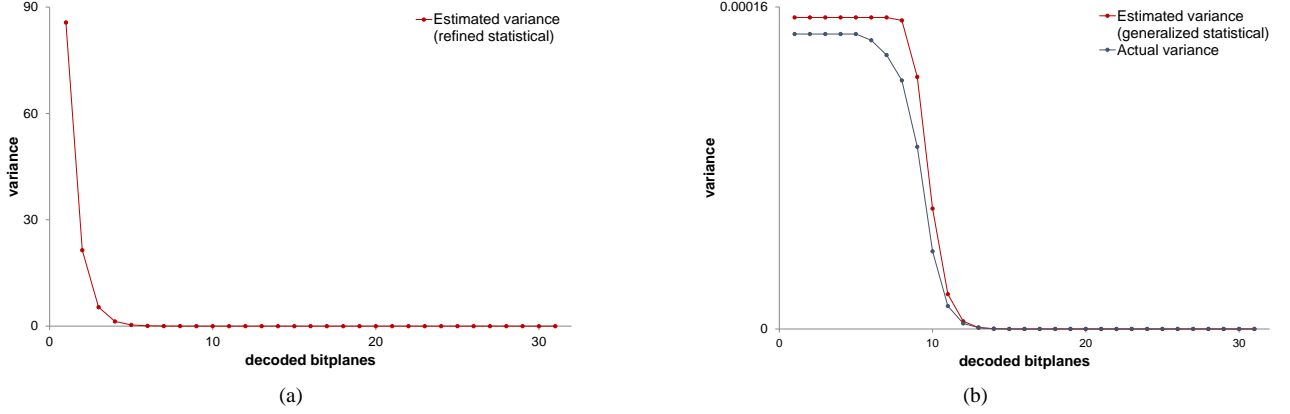


Figure 2: (a) Estimated variance with the refined statistical estimator; (b) Estimated variance with the generalized statistical estimator, and actual variance. All results are provided for the Dino model and highest resolution subband, when the number of bitplanes is equal across coordinates.

problem is convex and the solution can be determined using the method of Lagrange multipliers. The optimal distortion-rate slopes  $\lambda_j(b_j)$  are calculated using the bisection-method and have the following expression:

$$\lambda_j(b_j) = w_j \cdot \Delta D_{j,b_j} / \Delta R_{j,b_j} \quad (24)$$

where  $w_j$  are the weighting factors mentioned in (2), while  $\Delta R_{j,b_j}$  represents the actual increase in rate, and  $\Delta D_{j,b_j}$  denotes the decrease in distortion between two successive truncation points (i.e. subband bitplanes). The slopes  $\lambda_j(b_j)$  from all decomposition levels  $j$  and all bitplanes are sorted in a monotonically decreasing order. This corresponds to a global distortion-rate curve, and indicates the order in which the subbands have to be transmitted.

For comparison purposes with the original  $L_2$ -driven SIM codec [27], we have also considered the  $L_2$  distortion for the estimation of  $\Delta D_{j,b_j}$ . In this case, one refers to the classical high-rate approximation  $\Delta D_{j,b_j} = 2^{2b_j} \Delta_{j,0}^2 / 12$ . Similar to (6), this is a data-independent estimation. Moreover, it corresponds to a classical prioritization of subband bitplanes used in wavelet coding of images [20, 21, 53, 54], as well as for MeshGrid [17]. The weights  $w_j$  are numerically obtained such that the transform is approximately unitary, giving  $w_j = 2^{j-J}$ ,  $2 < j \leq J$  and  $w_1 = 1.25 \cdot 2^{1-J}$ .

In the  $L_\infty$  case, Table 1 includes for each MAXAD estimator the decrease in distortion  $\Delta D_{j,b_j}$ , and the subband weights  $w_j$ , provided for the unlifted Butterfly transform.

We note that the rate allocation for the estimators in sections III.A, III.B, and III.C is convex, as they all provide *convex* functions per subband. However, this comes at the expense of severely over-estimating the actual variance at very low rates (and, implicitly, the MAXAD via eq. (10) and (13)) – see an example in Figure 2(a). In contrast, the generalized statistical estimator in section III.D closely follows the actual variance – see Figure 2(b). However, one notices that the estimated (given by eq.(23)) and the actual error variances are non-convex. For this reason, the convex optimization method employed for the other three estimators does not apply to the generalized statistical estimator in the non-convex region. If employed, the generalized statistical

estimator generates non-competitive optimized distortion-rate functions.

However, we note that the variances and their estimates in Figure 2(b) are non-convex for the first 8-10 bitplanes, while their shape is similar to that of Figure 2(a) when sending more than 10 bitplanes. Also, the example of Figure 2(b) is quite extreme, as the transition between the non-convex and convex regions occurs earlier for lower resolution subbands, while the lowest resolution subbands do not exhibit this behavior at all.

So it is only for extremely low rates that the bitplane encoding order should be decided by solving a non-convex optimization problem, whereas for higher rates a convex solution would suffice. In the non-convex region, a simple solution would be for instance to exhaustively check all possible combinations for sending chunks of  $m$  bitplanes from the  $J$  subbands; this corresponds to  $J^m$  combinations to be evaluated, which is computationally light for small values of  $m$ . However, the non-convex region corresponds to extremely low rates, corresponding to very high MAXAD values, where the decoded objects are very deformed and not practically usable. Hence, to maintain a simple rate allocation, we have chosen to employ the generalized statistical estimator only as means to improve estimation accuracy, and to use a subband encoding order optimized with respect to one of the other three estimators.

#### IV. EXPERIMENTAL EVALUATION

We start the experimental section by testing the performance of the original ( $L_2$ -driven) SIM codec with respect to our proposed  $L_\infty$ -driven alternative, when employing either of the estimators presented in this paper. We note that a similar example has also been provided in [47, 48], and we only include it here for the sake of providing a complete analysis. We also include a similar comparison with respect to the state-of-the-art in semi-regular mesh coding, i.e. PGC [19].

Next, we investigate the rate-distortion performance of the three optimized progression (encoding) orders obtained with the MAXAD (i.e.  $L_\infty$  distortion) estimators in sections III.A, III.B, and III.C. As detailed at the end of the previous

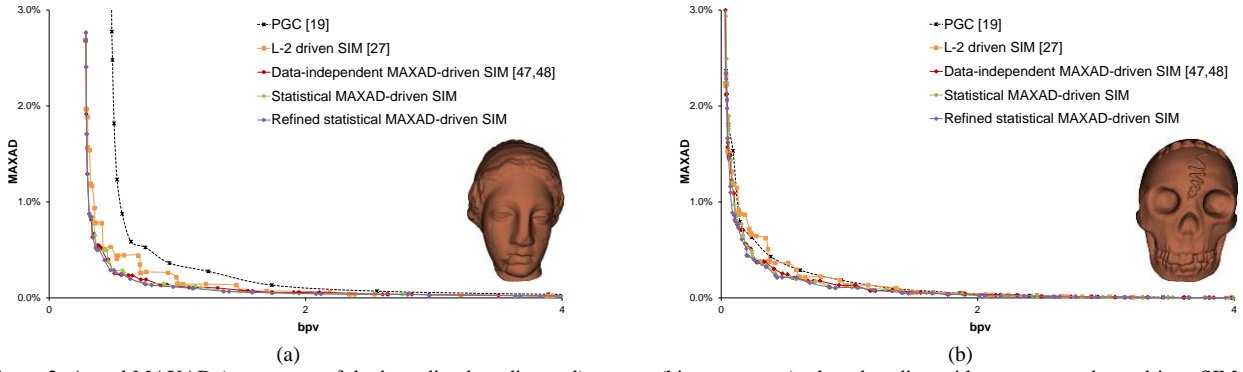


Figure 3: Actual MAXAD (percentage of the bounding box diagonal) vs. rate (bits per vertex) when decoding with our proposed  $L_\infty$ -driven SIM codec (as indicated by each of the proposed estimators), the original  $L_2$ -driven SIM codec [27] (predefined progression order), and PGC [19]. Vertex spikes can be seen for the  $L_2$ -driven SIM codec [27] both for the (non-normal) Venus and for the (normal) Skull mesh models.

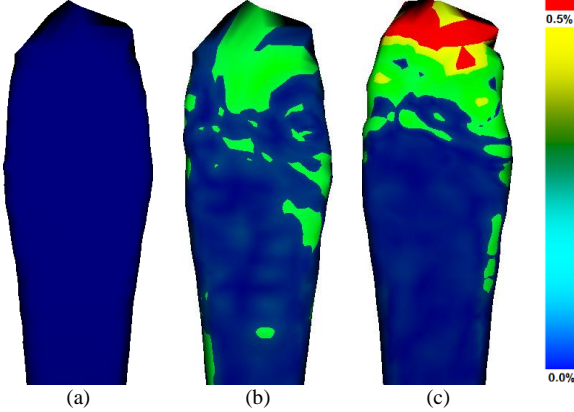


Figure 4: Screwdriver model (top part). (a) Original; (b) Decoded with the refined statistical  $L_\infty$ -driven SIM codec for a MAXAD upper bound of 0.5 % (of the bounding box diagonal), corresponding to a rate of 0.544 bpv, and (c) decoded with the original,  $L_2$ -driven SIM codec, for the same rate. Vertices whose reconstruction error exceeds the imposed bound are represented in red.

section, the generalized statistical estimator (section III.D) relies on either of these three progression orders. In the third set of experiments we compare the estimation accuracy of our proposed MAXAD estimators. In this sense, we will rely on both MAXAD formulations given in section II.A (see eq. (4), and eq. (5)). We end the section with a comparison between  $L_\infty$ -driven MeshGrid [46] codec, and our proposed  $L_\infty$ -driven semi-regular mesh codec.

In all experiments, the distortion will be given as a percentage (%) of the bounding box diagonal, whereas the rate will be given in bits per vertex (bpv).

#### IV.A. $L_\infty$ -driven vs. $L_2$ -driven mesh coding system

This first set of experiments is aimed at comparing the original  $L_2$ -driven implementation of the SIM codec [27] with the  $L_\infty$ -driven alternatives proposed in this paper. In this sense, Figure 3 depicts experimental results in terms of actual MAXAD versus bitrate for the (non-normal) Venus and the (normal) Skull mesh models. Each dot on the rate-distortion curves corresponds to a valid decoding point, where the local error is bounded and guaranteed. We observe from the graphs in Figure 3 that the original ( $L_2$  driven) SIM codec [27] is frequently prone to large vertex errors (“error spikes”). These are large vertex displacements that occur on one or more vertices due to quantization of the wavelet coefficients. This is to be expected in the case of the  $L_2$  metric, as it does not set bounds on the individual quantization errors.

In addition, we include in Figure 3 results corresponding to the PGC codec of [19]. As mentioned in section I.A, PGC [19] represents the state-of-the art in  $L_2$ -driven wavelet-based coding for semi-regular meshes. The rate

corresponding to the (uncompressed) base mesh is included in both cases. We remind that the PGC codec [19] only offers a quality scalable decoding order, which we use in these experiments. The results for the PGC codec [19] have been generated with the executables available online. It can be seen in both cases that PGC [19] has an inferior MAXAD vs. rate performance than our (proposed)  $L_\infty$ -driven SIM codec. With respect to the original  $L_2$ -driven SIM codec [27], PGC offers a lower MAXAD vs. rate performance for Venus, and a comparable one for Skull. We note that a full performance comparison between the PGC codec [19], and the (original)  $L_2$ -driven SIM codec [27] has been included in [27]. It was shown [27] that the original SIM codec outperforms the PGC codec in  $L_2$  sense.

Visually, one example of the “error spikes” that may occur in an  $L_2$ -driven codec is depicted in Figure 4 for the Screwdriver mesh model. The model is compressed employing our refined statistical  $L_\infty$ -driven SIM codec (i.e. optimized with respect to the estimator in section III.C), for a particular upper bound imposed on the MAXAD. Next, a decoded version is obtained for the same rate with the original ( $L_2$  driven) SIM codec. For comparison purposes, the original mesh is also depicted. In each case, vertices whose reconstruction error exceeds the MAXAD upper bound are represented in red, whereas the vertices whose reconstruction error respects the  $L_\infty$  upper bound are represented from blue to yellow, according to increasing magnitude. One observes in Figure 4 that such spikes may have an undesirable effect on the geometry of the mesh. The same effect was shown in [48]. Specifically, the geometry details may not be accurately preserved. For some applications (such as 3D gaming), this could easily be masked by the applied texture [55]. However certain applications (3D topography, 3D CAD, etc.) cannot benefit from such visual tricks. Each vertex position corresponds to a certain measurement and, hence, one requires control over the individual error.

#### IV.B. Rate-distortion performance

Using the rate-distortion optimization algorithm presented in section III.E, we obtain optimized subband encoding orders for the proposed estimators. The question now is which of the estimators yields the best rate-distortion performance. Looking again at Figure 3, we see that the rate-distortion curves often intersect. This may suggest that the actual rate-distortion performance of the proposed  $L_\infty$  distortion estimators is similar, and the differences between them are negligible. However, a better differentiation between the proposed  $L_\infty$  distortion estimators can be made by computing the area under their corresponding real (actual) distortion-rate curves. These areas under the graphs are reported in Table 2 and Table 3. As explained in section

TABLE 2

AREA UNDER THE REAL (ACTUAL) DISTORTION RATE GRAPHS. THE RESULTS ARE GIVEN FOR THE CASE WHEN THE NUMBER OF BITPLANES AT EACH DECODING POINT IS KEPT CONSTANT FOR EACH COORDINATE (MAXAD EVALUATED AS IN EQ. (4)).

Model		Data-independent [47, 48]	Statistical	Refined (and Generalized) statistical
Normal	Dino	0.57	0.61	<b>0.53</b>
	Screwdriver	0.57	0.56	<b>0.52</b>
	Skull	0.57	0.57	<b>0.51</b>
Non-Normal	Feline	0.37	0.36	<b>0.34</b>
	Rabbit	0.55	0.54	<b>0.49</b>
	Venus	0.49	0.47	<b>0.43</b>

TABLE 3

AREA UNDER THE REAL (ACTUAL) DISTORTION RATE GRAPHS. THE RESULTS ARE GIVEN FOR THE CASE WHEN THE NUMBER OF BITPLANES AT EACH DECODING POINT IS OPTIMIZED FOR EACH COORDINATE (MAXAD EVALUATED AS IN EQ. (5)).

Model		Data-independent [47, 48]			Statistical			Refined (and Generalized) statistical		
		x	y	z	x	y	z	x	y	z
Normal	Dino	0.15	0.15	0.18	0.14	0.14	0.18	<b>0.13</b>	<b>0.13</b>	<b>0.17</b>
	Screwdriver	0.17	0.17	0.12	0.17	0.17	0.12	<b>0.16</b>	<b>0.16</b>	<b>0.11</b>
	Skull	0.15	0.15	0.14	0.15	0.16	0.15	<b>0.14</b>	<b>0.14</b>	<b>0.14</b>
Non-Normal	Feline	0.09	0.08	0.11	0.41	0.09	0.11	<b>0.10</b>	<b>0.08</b>	<b>0.09</b>
	Rabbit	0.15	0.14	0.14	0.15	0.14	0.15	<b>0.14</b>	<b>0.13</b>	<b>0.14</b>
	Venus	0.12	0.12	0.12	0.12	0.12	0.13	<b>0.11</b>	<b>0.12</b>	<b>0.12</b>

III.E, the generalized statistical estimator is only used to improve estimation accuracy given an existing encoding order. Table 2 and Table 3 reveal that the subband encoding order provided by the refined data-dependent estimator proves to be the most competitive in rate-distortion sense. This order will be used in the subsequent experiments.

#### IV.C. Estimation accuracy

We are now interested in investigating the estimation accuracy of each proposed estimator. We recall that the variable  $P$  in eq. (13) expresses the probability with which the actual MAXAD is guaranteed to not exceed the estimated MAXAD.  $P$  is user-defined, and ideally,  $P=1$ . However  $P<1$ , and the closer the value of  $P$  is to 1, the larger is the difference between the estimated and the actual MAXAD values. This corresponds to decreasing the estimation accuracy. On the other hand, as the value of  $P$  increases, the uncertainty with which we estimate the actual MAXAD decreases. In other words, as  $P$  increases, we become more confident that the actual MAXAD does not exceed the estimated MAXAD.

An example of these curves for  $P = 1.0-10^{-18}$  is given in Figure 5. The subband coding order is predefined such that the real MAXAD vs. rate is common for all estimators. We chose the subband encoding order given by the refined statistical estimator, which was found to be the most competitive in rate-distortion sense (see the previous section). The blue curve depicts the actual (measured) MAXAD, i.e.  $L_\infty$  distortion, versus required rate for the (non-normal) *Rabbit* and (normal) *Dino* mesh models. To verify the accuracy of the estimation, we also plot the corresponding estimated MAXAD, for the same rate, given by each of the estimators proposed in this paper. The results show that the differences between the estimators are substantial at low-to-mid-rate ranges. Nevertheless, one points out that at high rates (larger than the 4 bpv depicted in Figure 5) all estimators provide accurate estimation of the actual MAXAD.

We would, however, like to provide an objective analysis concerning the accuracy of the proposed estimators. In this sense, we report the average rate penalties for various models, for different target MAXAD values, ranging from the maximum (corresponding to decoding only the base-mesh) to 0%. For each estimator and each target MAXAD, we compute the difference between the rate indicated by the

estimator and the actual rate needed to achieve this target. The rate allocation is optimized when imposing the same number of bitplanes across coordinates (corresponding to the MAXAD evaluation in eq. (4)) – see in Table 4. Table 5 reports similar results when separately optimizing the number of encoded bitplanes for each coordinate (corresponding to the MAXAD evaluation in eq. (5)). In both cases, one notices that the generalized statistical estimator significantly improves estimation accuracy. This is to be expected, as the generalized statistical estimator provides a faithful model of the real variance (see Figure 2 (b)) and, via eq. (13), of the MAXAD as well (see Figure 5).

#### IV.D. Comparison against $L_\infty$ -driven MeshGrid [46]

To the best of our knowledge, the only other  $L_\infty$ -driven mesh codec existing in the literature is MeshGrid [46]. However, compressing classical semi-regular 3D mesh models (e.g. *Dino*, *Skull*, *Rabbit* etc.) with MeshGrid involves a remeshing step, which will come with a corresponding remeshing error. Similarly, compressing MeshGrid 3D models such as *Humanoid* and *Heart* [46] will also require a remeshing procedure, in order to convert them to semi-regular meshes. Hence, directly comparing MeshGrid [46] to the  $L_\infty$ -driven semi-regular mesh codec proposed in this paper is not possible, as they operate on different types of meshes.

Still, we provide in Figure 6 a side-by-side comparison for two models originally created for MeshGrid, i.e. *Heart* ((a) and (b)) and *Humanoid* ((c) and (d)). Each system makes use of their corresponding version of the mesh models. Since neither MeshGrid model is compatible with the SIM codec, the necessary remeshing procedure was performed using the remesher of [56].

Figure 6 includes the actual  $L_\infty$  distortion versus rate, with both MeshGrid and the SIM codec, when optimizing each coding system with respect to their data-independent and statistical MAXAD estimators. The results corresponding to the  $L_\infty$ -driven MeshGrid system (Figure 6(a) and (c)) are the ones reported in [46]. For the SIM codec, we note that the base mesh has been losslessly encoded at 1.134 bpv for the *Heart* model, and at 0.287 bpv for the *Humanoid* model and is included in the rate reported at each decoded point. The MeshGrid system compresses all subbands resulting from the wavelet decomposition, including the coarsest approximation band.



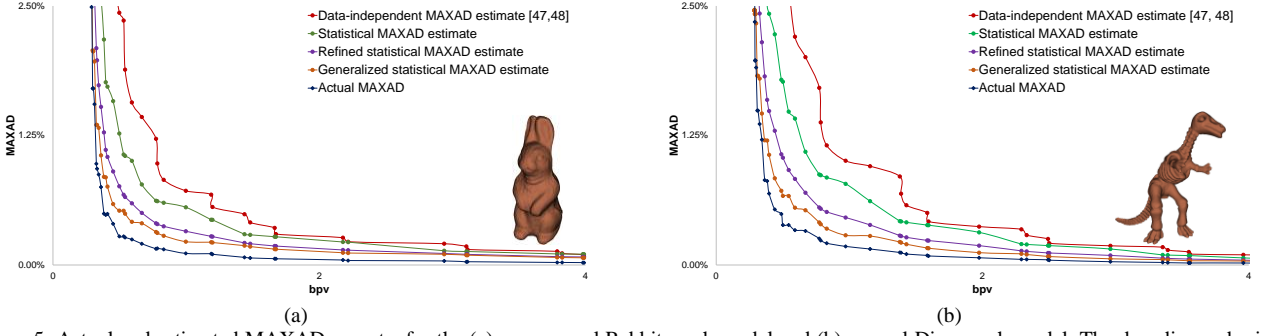


Figure 5: Actual and estimated MAXAD vs. rate, for the (a) non-normal Rabbit mesh model and (b) normal Dino mesh model. The decoding order is pre-determined, such that the actual MAXAD vs. rate, at each decoding point, is common to all estimators.

TABLE 4

AVERAGE RATE PENALTY (BPV) FOR VARIOUS MESH MODELS, CONSIDERING A CONSTANT NUMBER OF BITPLANES ACROSS COORDINATES AT EACH DECODING POINT AND  $P = 1.0 - 10^{-18}$ .

Model		Data-independent [47, 48]	Statistical	Refined Statistical	Generalized Statistical
Normal	Dino	0.658	0.417	0.191	<b>0.079</b>
	Screwdriver	0.433	0.252	0.121	<b>0.046</b>
	Skull	0.328	0.082	0.033	<b>0.007</b>
Non-Normal	Feline	0.416	0.229	0.103	<b>0.038</b>
	Rabbit	0.516	0.325	0.139	<b>0.072</b>
	Venus	0.472	0.27	0.111	<b>0.05</b>

TABLE 5

AVERAGE RATE PENALTY (BPV) FOR VARIOUS MESH MODELS, CONSIDERING AN OPTIMIZED NUMBER OF BITPLANES FOR EACH COORDINATE AT EACH DECODING POINT, AND  $P = 1.0 - 10^{-35}$ .

Model			Data-independent [47, 48]	Statistical	Refined statistical	Generalized statistical
Normal	Dino	x	0.154	0.138	0.065	<b>0.025</b>
		y	0.134	0.121	0.056	<b>0.028</b>
		z	0.157	0.146	0.066	<b>0.026</b>
	Screwdriver	x	0.109	0.087	0.039	<b>0.018</b>
		y	0.115	0.096	0.039	<b>0.007</b>
		z	0.078	0.057	0.025	<b>0.014</b>
	Skull	x	0.072	0.023	0.01	<b>0.003</b>
		y	0.079	0.026	0.012	<b>0.003</b>
		z	0.092	0.031	0.014	<b>0.004</b>
Non-Normal	Feline	x	0.105	0.083	0.032	<b>0.012</b>
		y	0.091	0.068	0.029	<b>0.013</b>
		z	0.118	0.09	0.033	<b>0.009</b>
	Rabbit	x	0.107	0.091	0.04	<b>0.017</b>
		y	0.123	0.111	0.048	<b>0.023</b>
		z	0.128	0.114	0.049	<b>0.023</b>
	Venus	x	0.114	0.091	0.038	<b>0.017</b>
		y	0.119	0.096	0.039	<b>0.023</b>
		z	0.097	0.082	0.035	<b>0.016</b>

## V. FUNCTIONALITIES

In this section we discuss the relation between the  $L_\infty$  distortion, and the Hausdorff distance. Moreover, we cover  $L_\infty$  scalability, and its relation to perceptual quality. Finally, we include a complexity evaluation of the  $L_\infty$ -driven coding system proposed in this paper.

### V.A. Relation to the Hausdorff distance

The Hausdorff distance computes the similarity between two meshes, being typically employed in mesh compression literature but also in other domains s.a. mesh simplification [57]. However, to our knowledge, there are no available algorithms that compute the Hausdorff distance in real time. For MeshGrid, the Hausdorff distance was proven to be upper bounded by the  $L_\infty$  distortion [58]. The same holds for the SIM codec, as we will show next. In line with the notations in section II, let  $V'$  be the set of decoded vertex positions  $v'_n \in V'$ , at a particular resolution and a given rate. Let us now consider  $V$  to be the set of losslessly decoded vertex positions  $v_n \in V$ , at the same resolution. Several remarks need to be made. First, a progressive refinement of the decoded vertex positions  $v'_n$  will eventually lead to the lossless counterpart  $v_n$ . Moreover, there is a bijective relation between  $V'$  and  $V$ , i.e. (i)  $\text{card}\{V'\} = \text{card}\{V\}$ ,

where  $\text{card}\{\cdot\}$  denotes the cardinality of the set, and (ii) for any losslessly reconstructed vertex  $v'_n \in V'$  there exists a unique corresponding vertex  $C(v'_n) \in V$ , such that  $C(v'_n) = v_n$  in the case of lossless reconstruction. The Hausdorff distance between  $V$  and  $V'$  is then defined as:

$$h(V, V') = \max_{v'_n \in V'} \left\{ \min_{v_n \in V} \{d(v_n, v'_n)\} \right\}$$

where  $d(v_n, v'_n)$  is any metric between  $v_n$  and  $v'_n$ . For the particular case of the Euclidean distance, one can write:

$$h(V, V') \leq \max_{v'_n \in V'} \{d(v_n, C(v'_n))\} = \text{MAXAD},$$

which is the same inequality as found in [58]. Table 6 reports the Hausdorff distance values obtained with the MESH tool [59], as well as the *actual*  $L_\infty$  distortion for various rates and several models, given three imposed upper bounds. As it can be observed, the  $L_\infty$  distortion provides a close upper bound for the Hausdorff distance. Hence, one can consider  $L_\infty$ -driven coding and Hausdorff distance coding of meshes practically equivalent, which is highly desirable in practice.

### V.B. $L_\infty$ scalability and relation to perceptual quality

Our proposed coding system supports scalability in  $L_\infty$  sense. That is, a lower-rate coded version of the input mesh

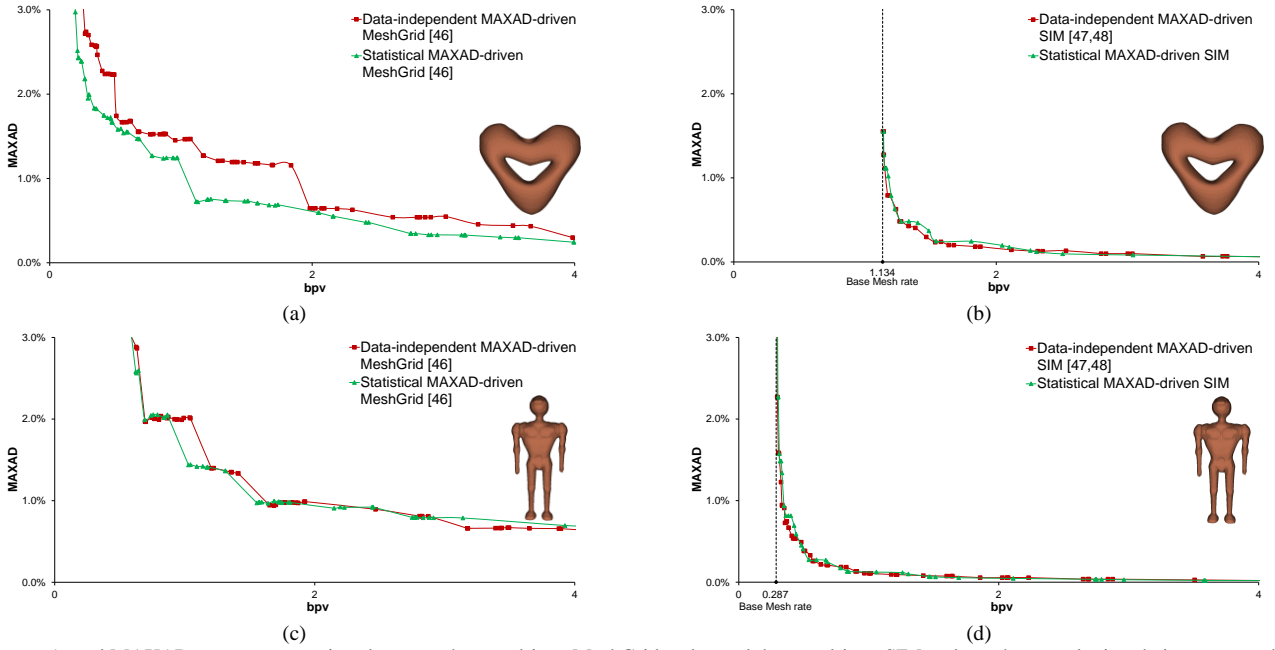


Figure 6: Actual MAXAD vs. rate comparison between the  $L_\infty$ -driven MeshGrid codec and the  $L_\infty$ -driven SIM codec, when employing their corresponding data-independent and statistical MAXAD estimators, respectively, for two MeshGrid mesh models.

TABLE 6  
HAUSDORFF DISTANCE (%) AND ACTUAL MAXAD VALUES (%) AT VARIOUS RATES (BPV), FOR DIFFERENT MESH MODELS.

Model	Imposed MAXAD	Actual MAXAD	Hausdorff distance	Rate
Normal	Dino	2.5%	1.97 %	0.29 bpv
		1.5%	1.36 %	0.33 bpv
		0.5%	0.34 %	0.59 bpv
	Screwdriver	2.5%	2.14 %	0.32 bpv
		1.5%	1.19 %	0.37 bpv
		0.5%	0.29 %	0.55 bpv
	Skull	2.5%	1.45 %	0.06 bpv
		1.5%	0.78 %	0.12 bpv
		0.5%	0.23 %	0.42 bpv
Non-Normal	Feline	2.5%	2.35 %	0.29 bpv
		1.5%	1.04 %	0.32 bpv
		0.5%	0.31 %	0.51 bpv
	Rabbit	2.5%	1.70 %	0.30 bpv
		1.5%	0.98 %	0.33 bpv
		0.5%	0.28 %	0.50 bpv
	Venus	2.5%	2.41 %	0.29 bpv
		1.5%	0.88 %	0.31 bpv
		0.5%	0.29 %	0.48 bpv

is a prefix of a higher-rate version. Moreover, for each allowable truncation point, i.e. each decoding point, the MAXAD ( $L_\infty$  distortion) is bounded. We note that this is a lossy-to-lossless coding approach which can progressively reconstruct the input mesh up to its lossless version.

An example is given in Figure 7, where the *Skull* mesh model passes from being highly distorted (corresponding to large values of the  $L_\infty$  upper bound), to lossless reconstruction (corresponding to an  $L_\infty$  upper bound equal to 0% of the diagonal of the bounding box). One observes that (i) the quality is progressively improved as the rate is increased, and (ii) the  $L_\infty$  distortion is bounded at each decoding point. This corresponds to  $L_\infty$  scalability, which is a unique feature in semi-regular mesh coding.

We remind that an  $L_2$ -driven codec cannot claim to preserve geometry details, as it is frequently prone to “error spikes”. This was discussed in section IV.A and depicted in Figure 4. Still, there is no indication that an  $L_2$ -driven codec necessarily provides lower perceptual quality than its  $L_\infty$ -driven alternative. For this reason, we would like to compare the perceptual quality offered by our proposed  $L_\infty$ -driven SIM codec (when optimized with respect to the refined statistical estimator), to that offered by the (original)  $L_2$ -driven SIM codec [27]. In this sense, we rely on the MSDM metric of Lavoué et al. [60], and use the losslessly decoded

mesh as a reference. The results of this comparison are given in Table 7 for a pool of  $L_\infty$  upper bounds. We note that  $MSDM(X, Y) \in [0, 1]$  [60], for any two meshes  $X$  and  $Y$ . The MSDM values decrease with the differences in perceptual quality between  $X$  and  $Y$ , with 0 indicating identical meshes. One notices in Table 7 that decreasing the imposed  $L_\infty$  bound increases the perceptual quality of the mesh. Moreover, the proposed  $L_\infty$ -driven SIM codec offers better perceptual quality than the (original)  $L_2$ -driven codec [27], in the vast majority of cases. We note that we are the first to provide a comparison in terms of perceptual quality between an  $L_2$ -driven codec and its  $L_\infty$ -driven alternative.

#### V.C. Complexity Evaluation

In order to assess the time complexity of the proposed  $L_\infty$ -driven coding system, execution-time tests were conducted employing executables generated by Visual Studio 2010 operating in release mode. The source code was written in C++. All tests were conducted on a notebook with an Intel Core i7-4940MX CPU at 3.10 GHz, 32 GB of RAM, and operating system Windows 8.1.

Table 8 reports encoding, Laplacian Mix PDF fitting, post compression rate-distortion optimization (PCRD), and decoding times, for 6 mesh models. Unlike the results presented in [27], the encoding time here includes the

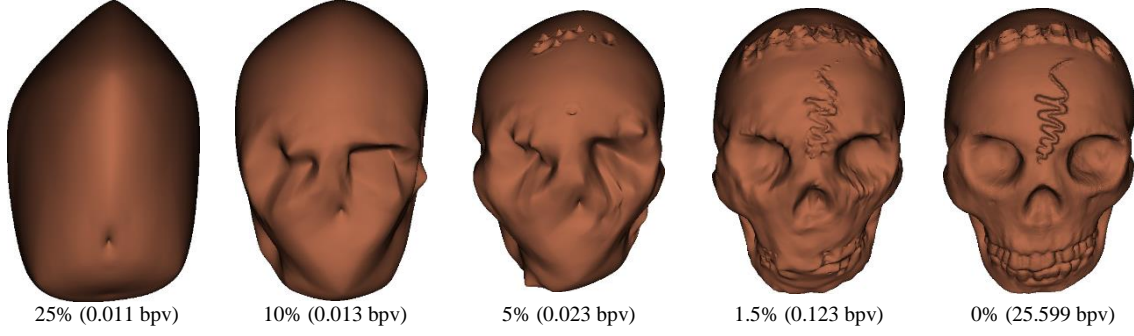


Figure 7:  $L_\infty$  scalability provided by the proposed approach. Skull mesh model decoded at various target MAXAD ( $L_\infty$  distortion) bounds when using the refined statistical estimator. The estimated MAXAD (in % of the bounding box diagonal) and the required rate are indicated under each decoded version.

TABLE 7

MSDM [60] VALUES OBTAINED WITH THE PROPOSED  $L_\infty$ -DRIVEN CODEC (WHEN USING THE REFINED STATISTICAL ESTIMATOR), AND WITH THE ORIGINAL  $L_2$ -DRIVEN IMPLEMENTATION OF [27]. THE VALUES ARE GIVEN FOR THE SKULL MESH MODEL.

$L_\infty$ bound	Rate (bpv)	MSDM with proposed $L_\infty$ -driven codec	MSDM with original $L_2$ -driven codec of [27]
10%	0.013	0.63201	0.62610
5%	0.023	0.56980	0.57424
4.5%	0.025	0.56895	0.56847
4%	0.034	0.54856	0.55310
3.5%	0.039	0.54343	0.55162
3%	0.046	0.52637	0.53970
2.5%	0.058	0.51008	0.52321
2%	0.088	0.46572	0.48436
1.5%	0.123	0.45504	0.46620
1%	0.196	0.39813	0.43066
0.5%	0.425	0.32093	0.32949

TABLE 8

EXECUTION TIMES (IN SECONDS) FOR THE PROPOSED  $L_\infty$ -DRIVEN SYSTEM

Model (#vertices)		Dino (129026)	Screwdriver (65538)	Skull (131074)	Feline (258046)	Rabbit (107522)	Venus (198658)	Average
Encoding		1.81	0.97	1.72	3.58	1.51	2.54	<b>2.02</b>
PDF fitting		1.47	0.34	0.69	2.35	5.91	6.84	<b>2.93</b>
PCRD	Deterministic	2.04	1.26	1.73	3.62	1.86	3.31	<b>2.30</b>
	Statistical	2.05	1.28	1.78	3.64	2.04	3.38	<b>2.36</b>
	Refined Stat.	2.53	1.51	1.96	4.11	2.23	3.79	<b>2.69</b>
Decoding	Deterministic	1.34	0.73	1.06	3.00	1.32	2.68	<b>1.69</b>
	Statistical	1.33	0.72	1.05	3.00	1.35	2.67	<b>1.69</b>
	Refined Stat.	1.34	0.72	1.01	3.00	1.34	2.67	<b>1.68</b>

transform as well, which introduces the largest time penalties. Note that the PDF fitting is only required by the refined (section III.C), and the generalized (section III.D) statistical estimator. With respect to the PCRD algorithm (section III.E), the biggest time penalties are brought by computing the real rates used in eq. (24); computing the estimated distortion is instantaneous (maximum 0.001s), while generating the global rate-distortion optimal curve requires maximum 0.019s across models, and estimators. Note that the PDF fitting, and the PCRD need to be performed only once, and offline. At runtime, given the global rate-distortion optimal curve, parsing the bitstream according to the imposed upper bound on the MAXAD is instantaneous. Finally, we note that we have included maximum decoding times (lossless reconstruction, i.e. last point on the global R-D curve).

## VI. CONCLUSIONS AND FUTURE WORK

To our knowledge, this paper introduces the only  $L_\infty$ -driven semi-regular mesh geometry coding system in the literature. We continue our work in [47, 48] and introduce novel data-dependent estimators which substantially improve estimation accuracy at low rates. Our system also allows a variable number of bitplanes to be decoded from each coordinate, increasing the granularity and allowing for independently controlling the local coding error along each direction. Moreover, experiments show that the  $L_\infty$  distortion is a tight upper bound for the Hausdorff distance.

Hence, our proposed  $L_\infty$  coding approach actually implies Hausdorff distance-constrained coding, which is highly desirable in practice. The proposed coding paradigm provides scalability in  $L_\infty$ -sense and better perceptual quality than its  $L_2$ -driven alternative.

Our system has several limitations. Firstly, the attributes require separate coding. In the particular case of texture compression, one can rely on the DXT family. Alternatively, one can employ our recently-published wavelet-based texture coding system [61]. An  $L_\infty$ -driven extension might borrow concepts from the approach presented in this paper or past work on images [45]. Secondly our system targets semi-regular meshes. The alternative is to employ irregular meshes, and to devise  $L_\infty$  codecs for such systems. In this sense, we have recently published a wavelet-based irregular mesh codec [62], for which one could envisage devising  $L_\infty$  coding approaches. However, the transform devised in [62] is *adaptive*, and very different with respect to the classical Butterfly [49] transform used for semi-regular meshes. Hence,  $L_\infty$  coding of irregular meshes is a subject in its own, which we will exploit in the future.

## ACKNOWLEDGEMENTS

The authors would like to thank the anonymous reviewers for their constructive remarks and suggestions. The work in this paper has been supported by the 3DLicornea project funded by the Brussels Region (Brussels Institute for Research and Innovation – Innoviris).

## REFERENCES

- [1] C. L. Bajaj, V. Pascucci, and G. Zhuang, "Compression and coding of large CAD models," University of Texas, Technical Report 1998.
- [2] R. Mekuria, M. Sanna, E. Izquierdo, D. C. A. Bulterman, and P. Cesar, "Enabling Geometry-Based 3-D Tele-Immersion With Fast Mesh Compression and Linear Rateless Coding," *IEEE Trans. on Multimedia*, vol. 16, pp. 1809 - 1820, 2014.
- [3] G. H. Weber, P.-T. Bremer, and V. Pascucci, "Topological landscapes: a terrain metaphor for scientific data," *IEEE Trans. on Vis. and Computer Graphics*, vol. 13, pp. 1416-1423, 2007.
- [4] A. G. Bors, "Watermarking mesh-based representations of 3-D objects using local moments," *IEEE Trans. on Image Processing*, vol. 15, pp. 687 - 701, March 2006.
- [5] M.-S. Kim, S. Valette, H.-Y. Jung, and R. Prost, "Watermarking of 3D irregular meshes based on wavelet multiresolution analysis," *Lecture Notes on Computer Science*, pp. 313-324, 2005.
- [6] B. Vasic and B. Vasic, "Simplification Resilient LDPC-Coded Sparse-QIM Watermarking for 3D-Meshes," *IEEE Trans. on Multimedia*, vol. 15, pp. 1532 - 1542, 2013.
- [7] P. Hammond, "The use of 3D face shape modelling in dysmorphology," *Archives of Disease in Childhood*, vol. 92, pp. 1120-1126, 2007.
- [8] J. Rossignac and P. Borrel, "Multi-resolution 3D approximation for rendering complex scenes," *Geometric Modeling in Computer Graphics*, pp. 445-465, 1993.
- [9] M. Soucy and D. Laurendeau, "Multiresolution surface modelling based on hierarchical triangulation," *Computer Vision and Image Understanding*, vol. 63, pp. 1-14, 1996.
- [10] R. Ronfard and J. Rossignac, "Full-range approximation of triangulated polyhedra," *Proc. of Eurographics, Computer graphics forum*, vol. 15, pp. C67-C76, 1996.
- [11] M. Garland and Heckbert, "Surface simplification using quadric error metrics," presented at the SIGGRAPH, 1997.
- [12] J. Li and C.-C. J. Kuo, "Progressive coding of 3-D graphic models," *Proc. of the IEEE*, vol. 86, pp. 1052-1063, 1998.
- [13] R. Pajarola and J. Rossignac, "Compressed Progressive Meshes," *IEEE Trans. on Circuits and Systems for Video Technology*, vol. 6, pp. 79-93, 2000.
- [14] G. Taubin, A. Guezic, W. Horn, and F. Lazarus, "Progressive forest split compression," *ACM SIGGRAPH*, pp. 123-132, 1998.
- [15] S. Valette, R. Chaine, and R. Prost, "Progressive lossless mesh compression via incremental parametric refinement," *Computer Graphics Forum*, vol. 28, pp. 1301-1310, 2009.
- [16] J. Peng, Y. Huang, C. C. J. Kuo, I. Eckstein, and M. Gopi, "Feature oriented progressive lossless mesh coding," *Computer Graphics Forum*, vol. 29, pp. 2029-2038, 2010.
- [17] I. A. Salomie, A. Munteanu, A. Gavrilescu, G. Lafruit, P. Schelkens, R. Deklerck, et al., "MeshGrid - a compact, multi-scalable and animation-friendly surface representation," *IEEE Trans. on Circuits and Systems for Video Technology*, vol. 14, pp. 950-966, 2004.
- [18] M. Lounsbery, T. D. Deroose, and J. Warren, "Multiresolution analysis for surfaces of arbitrary topological type," *ACM Trans. on Graphics*, vol. 16, pp. 34-73, 1997.
- [19] A. Khodakovsky, P. Schroder, and W. Sweldens, "Progressive geometry compression," *Proc. of SIGGRAPH*, 2000.
- [20] J. M. Shapiro, "Embedded image coding using zerotrees of wavelet coefficients," *IEEE Trans. on Signal Processing*, vol. 41, pp. 3445-3462, 1993.
- [21] A. Said and A. W. Pearlman, "A new fast and efficient image codec based on set partitioning in hierarchical trees," *IEEE Trans. on Circuits and Systems for Video Technology*, vol. 6, pp. 243-250, 1996.
- [22] A. Khodakovsky and I. Guskov, *Compression of normal meshes*: Springer-Verlag, 2003.
- [23] I. Guskov, K. Vidmce, W. Sweldens, and P. Schroder, "Normal meshes," in *ACM SIGGRAPH*, New Orleans, Louisiana, USA, 2000, pp. 95-102.
- [24] M. Aviles, F. Moran, and G. Narciso, *Progressive Lower Trees of Wavelet Coefficients: Efficient Spatial and SNR Scalable Coding of 3D Models* vol. 3767: Springer Berlin / Heidelberg, 2005.
- [25] F. Payan and M. Antonini, "Mean square error approximation for wavelet-based semiregular mesh compression," *IEEE Trans. on Vis. and Computer Graphics*, vol. 12, pp. 649-657, 2006.
- [26] F. Payan and M. Antonini, "An efficient bit allocation for compressing normal meshes with an error-driven quantization," *Computer Aided Geometric Design*, vol. 22, pp. 466-486, 2005.
- [27] L. Denis, S.-M. Satti, A. Munteanu, J. Cornelis, and P. Schelkens, "Scalable intraband and composite wavelet-based coding of meshes," *IEEE Trans. on Multimedia*, vol. 12, pp. 773-789, 2010.
- [28] J. Peng, C.-S. Kim, and C.-C. Jay Kuo, "Technologies for 3D mesh compression: A survey," *Elsevier Journal of Visual Communication and Image Representation*, vol. 16, pp. 668-733, 2005.
- [29] D. Berjon, F. Moran, and S. Manjunatha, "Objective and subjective evaluation of static 3D mesh compression," *Elsevier Signal Processing: Image Communication*, vol. 28, pp. 181-195, 2013.
- [30] G. AlRegib, Y. Altunbasak, and J. Rossignac, "Error-resilient transmission of 3-D models," *ACM Trans. on Graphics*, vol. 24, pp. 182-208, 2005.
- [31] D. Tian and G. AlRegib, "Multistreaming of 3-D scenes with optimized transmission and rendering scalability," *IEEE Trans. on Multimedia*, vol. 9, 2007.
- [32] S.-B. Park, C.-S. Kim, and S.-U. Lee, "Error resilient 3-D mesh compression," *IEEE Trans. on Multimedia*, vol. 8, pp. 885-895, 2006.
- [33] F. Moran and N. Garcia, "Comparison of wavelet-based 3-D model coding techniques," *IEEE Trans. on Circuits and Systems for Video Technology*, vol. 14, pp. 937-949, 2004.
- [34] J.-K. Ahn, Y. J. Koh, and C.-S. Kim, "Efficient Fine-Granular Scalable Coding of 3D Mesh Sequences " *IEEE Trans. on Multimedia*, vol. 15, pp. 485 - 497, 2013.
- [35] K. Chen and T. V. Ramabadran, "Near-lossless compression of medical images through entropy-coded DPCM," *IEEE Trans. on Medical Imaging*, vol. 13, pp. 538-548, 1994.
- [36] L. Ke and M. W. Marcellin, "Near-lossless image compression: minimum-entropy, constrained-error DPCM," *IEEE Trans. on Image Processing*, vol. 7, pp. 225 - 228, 1998.
- [37] X. Wu, N. Memon, and K. Sayood, "A Context-Based, Adaptive, Lossless/Near-Lossless Coding Scheme for Continuous-Tone Images," France Patent, 1996.
- [38] X. Wu and N. Memon, "Context-based, adaptive, lossless image coding," *IEEE Trans. on Communications*, vol. 45, pp. 437-444, 1997.
- [39] X. Wu and P. Bao, "L-infinity-constrained high-fidelity image compression via adaptive context modeling," *IEEE Trans. on Image Processing*, vol. 9, pp. 536-542, 2000.
- [40] I. Avcibas, N. Memon, B. Sankur, and K. Sayood, "A progressive lossless/near-lossless image compression algorithm," *IEEE Signal Processing Letters*, vol. 9, pp. 312-314, 2002.
- [41] L. Karray, P. Duhamel, and O. Rioul, "Image coding with an  $L^\infty$  norm and confidence interval criteria " *IEEE Trans. on Image Processing*, vol. 7, pp. 621 - 631, 1998.
- [42] R. Ansari, N. Memon, and E. Ceran, "Near-lossless image compression techniques," *Journal of Electronic Imaging*, vol. 7, pp. 486-494, 1998.
- [43] S. Chuah, S. Dumitrescu, and X. Wu, "l2 optimized predictive image coding with  $l^\infty$  bound," *IEEE Trans. on Image Processing*, vol. 22, pp. 5271-5281, 2013.
- [44] A. Alecu, A. Munteanu, J. Cornelis, and S. Dewitte, "On the optimality of embedded deadzone scalar-quantizers for wavelet-based L-infinity-constrained image coding," *IEEE Signal Processing Letters*, vol. 11, pp. 367-371, 2004.
- [45] A. Alecu, A. Munteanu, J. Cornelis, and P. Schelkens, "Wavelet-based scalable L-infinity-oriented compression," *IEEE Trans. on Image Processing*, vol. 15, 2006.
- [46] A. Munteanu, D. C. Cernea, A. Alecu, J. Cornelis, and P. Schelkens, "Scalable L-Infinity coding of meshes," *IEEE Trans. on Visualization and Computer Graphics*, vol. 16, pp. 513-528, 2010.
- [47] R. Florea, L. Denis, J. Lievens, A. Munteanu, and P. Schelkens, "Theoretical distortion estimation in L-infinity wavelet-based coding of semi-regular meshes," in *EU/SIPCO*, Bucharest, RO, 2012.
- [48] R. Florea, L. Denis, J. Lievens, A. Munteanu, and P. Schelkens, "L-infinity coding of 3D representations of human affect," in *ICME*, Melbourne, AU, 2012.
- [49] N. Dyn, D. Levine, and J. A. Gregory, "A butterfly subdivision scheme for surface interpolation with tension control," *ACM Trans. on Graphics*, vol. 9, pp. 160-169, 1990.
- [50] C. Touma and C. Gotsman, "Triangle mesh compression," in *Proc. of Graphics Interface*, Vancouver, 1998.
- [51] D. S. Taubman and M. W. Marcellin, *JPEG2000: Image compression fundamental, standards and practice*. Dordrecht: Kluwer Academic Publishers, 2001.
- [52] A. Papoulis, *Probability, Random Variables, and Stochastic Processes*. NY: McGraw-Hill, 1964.
- [53] A. Munteanu, J. Cornelis, G. Van der Auwera, and P. Cristea, "Wavelet-based lossless compression scheme with progressive transmission capability," *International Journal of Imaging Systems and Technology, Special Issue on Image and Video Coding*, vol. 10, pp. 76-85, 1999.
- [54] A. Munteanu, J. Cornelis, G. Van der Auwera, and P. Cristea, "Wavelet image compression - the quadtree coding approach," *IEEE Trans. on Information Technology in Biomedicine*, vol. 3, pp. 176-185, 1999.
- [55] G. Lavoue and M. Corsini, "A Comparison of Perceptually-Based Metrics for Objective Evaluation of Geometry Processing," *IEEE Trans. on Multimedia*, vol. 12, pp. 636 - 649, 2010.
- [56] I. Guskov, "Manifold-based approach to semi-regular remeshing," *Graphical Models*, vol. 69, pp. 1-18, 2007.
- [57] R. Klein, G. Liebich, and W. Straßer, "Mesh reduction with error control," *Proc. of IEEE Visualization*, pp. 311-318, 1996.
- [58] D. C. Cernea, A. Munteanu, A. Alecu, J. Cornelis, and P. Schelkens, "Scalable joint source and channel coding of meshes," *IEEE Trans. on Multimedia*, vol. 10, pp. 503-513, 2008.
- [59] N. Aspert, D. Santa-Cruz, and T. Ebrahimi, "MESH: Measuring error between surfaces using the Hausdorff distance," in *ICME*, 2002, pp. 705-708.
- [60] G. Lavoue, E. D. Gelasca, F. Dupont, A. Baskurt, and T. Ebrahimi, "Perceptually driven 3D distance metrics with application to watermarking " presented at the SPIE Applications of Digital Image Processing, San Diego, 2006.
- [61] B. Andries, J. Lemeire, and A. Munteanu, "Scalable texture compression using the wavelet transform," *The Visual Computer*, pp. 1-19, 2016.
- [62] J. El Sayeh Khalil, A. Munteanu, L. Denis, P. Lambert, and R. Van de Walle, "Scalable Feature-Preserving Irregular Mesh Coding," *Computer Graphics Forum*, pp. 1-17, 2016.